Materials Today Communications 36 (2023) 106456

Contents lists available at ScienceDirect

Materials Today Communications

journal homepage: www.elsevier.com/locate/mtcomm

Mechanical characterisation of 3D printed lightweight lattice structures with varying internal design alterations

James J. Lee [a,*], Ali A. Mohammed [b], Andy Pullen [c], Connor W. Myant [b], William G. Proud [a]

[a] Institute of Shock Physics, Department of Physics, Imperial College London, SW7 2AZ London, UK
[b] Faculty of Engineering, Dyson School of Design Engineering, Imperial College London, SW7 2AZ London, UK
[c] Department of Civil and Environmental Engineering, Imperial College London, SW7 2AZ London, UK

ARTICLE INFO

Keywords:
3D printing
Vat photopolymerisation
Flexible material
Energy absorption
Lattice structure
Mechanical characterisation

ABSTRACT

The recent advances in the additive manufacturing (AM) have enhanced the development of light-weight, energy-absorbing structures in many aspects with precise, designed configurations of the internal structure. Given the range of potential materials many possible variations exist compared to the existing polymer-based foams. The advantages of rapid prototyping, enabled through AM, allows a streamlined process in obtaining a structure of desired mechanical behaviour. In this work, development, and design variation of a flexible lattice structure with core strut modification is demonstrated. The core struts are varied in terms of shape and density and are fabricated using vat photopolymerisation with Formlabs Flexible 80A resin and experimental methodology is outlined for the characterisation of the printed specimen under compressive loading. Mechanical characterisation under three different compression rates presents that the implementation of the core strut increases the elastic modulus of the lattice structure. The enhanced stiffness effects are further increased with the variations in shape, while the evaluation of the density variations shows significantly different deformation behaviour and strain rate sensitivity. The behaviour of each specimen types is discussed further in terms of their functional viability and potential applications where the design specific behaviour and small, lightweight form factor can be most effectively utilised.

1. Introduction

The recent advances in additive manufacturing (AM) have enhanced the development of lightweight, energy-absorbing structures in many aspects with precise, designed configurations of the internal structure [1,2]. Given the range of potential materials many possible variations exist compared to the existing materials conventionally deployed for energy-absorbing purposes. The advantages of rapid prototyping, enabled through AM, allows a streamlined process in obtaining a structure of desired mechanical behaviour.

The need for lightweight energy-absorbing materials exists in many areas where a protection of fragile or sensitive subject is crucial. This includes military settings, where a lightweight and accessible energy-absorbing structures are crucial in providing critical protection of vital infrastructure and secure transportation of energetic materials [3]. Another area where application of dimensionally efficient energy-absorbing designs has significance is in automotive and aerospace industry [4,5]. One example is the seats within elite motor sport vehicles, such as Formula 1 racing. The seat material must provide sufficient comfort and protection from multi-directional loading of different levels, from constant vibrations to a high-level stress, while minimising its weight and size.

Amongst the wide variety of AM technologies capable of creating complex structures, vat photopolymerisation has become one of the most commonly used 3D printing processes across commercial, industrial and research applications. Vat photopolymerisation utilises a photo-curable resin that solidifies when polymerised using a UV laser light source, normally with a wavelength between 300 and 405 nm. The layer-by-layer manufacturing process deployed by vat photopolymerisation is capable of achieving higher resolutions than Fused Deposition Modelling (FDM) and Fused Filament Fabrication (FFF), therefore suited for creating complex lattice structures with minimal size features. The advantages of using have been deployed in several technological fields such as medical implants and tissue engineering, aeronautical, naval, and automotive engineering [6–9].

This study presents a process of developing lightweight energy-

* Correspondence to: Institute of Shock Physics, Department of Physics, Imperial College London, South Kensington Campus, SW7 2AZ, UK.
E-mail address: james.lee11@imperial.ac.uk (J.J. Lee).

https://doi.org/10.1016/j.mtcomm.2023.106456
Received 21 April 2023; Received in revised form 7 June 2023; Accepted 13 June 2023
Available online 15 June 2023

absorbing lattice structures, utilising the capabilities allowed by vat photopolymerisation including fine-tuning of internal architecture of the materials which is not possible for the conventionally used chemically manufactured foams such as polyurethane. Through iterative design process on the internal features of the lattices and the experimental investigation of their performances, a flexible and fast development cycle will be demonstrated.

The study on variations of lattice structure designs in the context of additive manufacturing is a very actively investigated area with increasing interest. Over the years, several variables in the lattice structure design have been identified that affect their mechanical properties and deformation behaviour. The features that have been mainly focused by the existing literature include relative density, the size, and the geometry of the unit cell [10–14]. To date, the lattice structures that are additively manufactured and mechanically characterised are mostly composed of strut-based cells, such as body-centred-cubic (BCC) and face-centred-cubic (FCC) and their variations [12,15–17].

This study looks to expand on the research of mechanical properties of lattice structures with strut-based cells, by consideration of more complex unit-cell configuration and modification of the internal designs. For this purpose, a sandwich structure with re-entrant honeycomb-based lattice core will be considered as the reference structure [18]. Modifications will be made primarily in the form of implementing an additional strut in the core of the lattice where the initial design is empirically resolved to deform by axial folding. Further iterations to this core strut will be considered in terms of density and shape as well as the arrangement of the struts within the lattice. Each variant of the will be mechanically characterised under compression at varying loading rates, in order to investigate the effects of structural modification of lattices on the mechanical response.

The key aims of this study can be summarised as: 1) Demonstrate the precision achieved using the vat photopolymerisation with a soft, flexible resin through the optimisation processes to fabricate light-weight structures of relatively small sizes. 2) Investigate the effects of variation in the design of specific components within the structure on the response. A sandwich structure with re-entrant honeycomb-based core is chosen as a base architecture and modifications are implemented with the concept of core struts of different variants. 3) Present the development of experimental diagnostics to test and measure the response of soft materials under varying degrees of strain rate regimes.

2. Materials and methods

A lattice structure based on re-entrant honeycomb unit cell was chosen as the base design for this study. Re-entrant honeycomb lattice is an auxetic structure that exhibit negative Poisson's ratios such that, upon compression they show lateral reduction in volume unlike regular cellular structures [18]. This behaviour shows enhancements in shear stiffness, compression, and impact resistance which contributes to the improved energy absorption of the structure [19,20].

2.1. Re-entrant honeycomb structure

The 3D lattice structure used in this study is based on a 2D re-entrant honeycomb first proposed by Almgren, presented Fig. 1 [21]. The values of the parameters V, H and θ are shown in Table 1. The values were determined empirically through a series of preliminary manufacturing and testing cycles until an appropriate design suitable for the desired purpose was achieved. The process considered factors such as: the precision of the 3D printer, structural integrity of the sample with the resin material, dimensions of the testing platform, and the sensitivity of the experimental diagnostics.

2.1.1. 3D lattice structure

A 3D version of the unit cell was produced using a CAD software (Fusion360, Autodesk) and, following the arrangement depicted in Fig 1, lattice structure was constructed as shown in Fig. 2. Fig. 2(a) shows the 2D side-view of the unit cell where the struts follow the parameters listed in Table 1. The isometric views of the 3D unit cell and the lattice constructed by linkage of the unit cells are presented in Fig. 2(b) and (c), respectively. All of the lattice structures used throughout the study were 4 layers with each layer consisting of 6 × 6-unit cells.

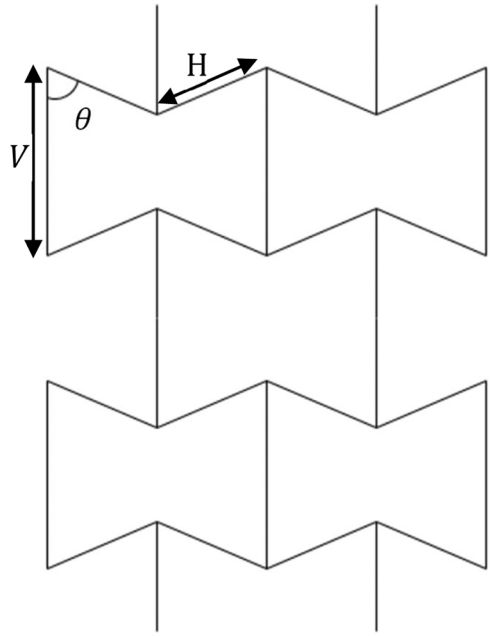

Fig 1. 2D Unit cell arrangement.

Table 1
Design parameters of the re-entrant honeycomb unit cell.

Parameters	
V	1.8 mm
H	1.1 mm
θ	73°

2.1.2. Sandwich structure configuration

The final design opted for this study is a sandwich structure with two thick panels, relative to the cell struts, with the re-entrant honeycomb lattice core. All of the components of the structure were made from the same printer resin.

Such configuration was chosen to enhance resistance to any compression in the lateral direction with additional advantages of preventing unwanted wear and tear of the thin struts during storage and transportation. The panels also allow for structural stability during the printing process, removing any overhanging features in the design and holding the thin struts in place which otherwise may fail due to the small size of the struts and the relatively low strength of the resin material. The printed, and post-cured, sandwich structure is shown in Fig. 3.

2.1.3. Mechanical response to compression

Some preliminary compression testing of the printed samples was carried out. Under low rate compression (in the range of 10^{-3} s^{-1} strain rate) in the axial direction, perpendicular to the plane of the sandwich panel, the response of the lattice structure exhibited an expected stress-strain behaviour of materials such as foam and other cellular structures [22].

As shown in Fig. 4, the response is characterised in three distinctive phases: linear elastic, stress plateau, and densification phase; where

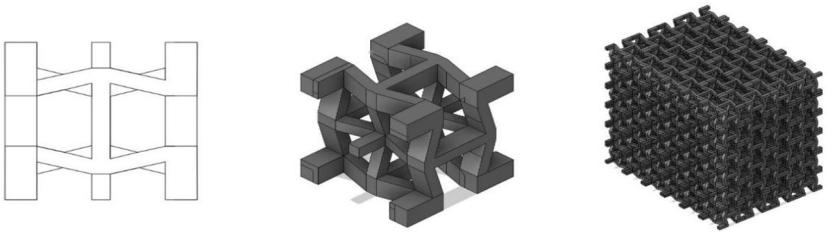

(a) 2D side view of the unit cell (b) 3D unit cell (c) 3D lattice

Fig. 2. Re-entrant honeycomb unit cell and lattice.

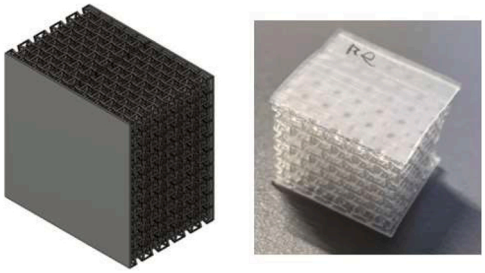

Fig. 3. 3D printed re-entrant honeycomb core sandwich structure.

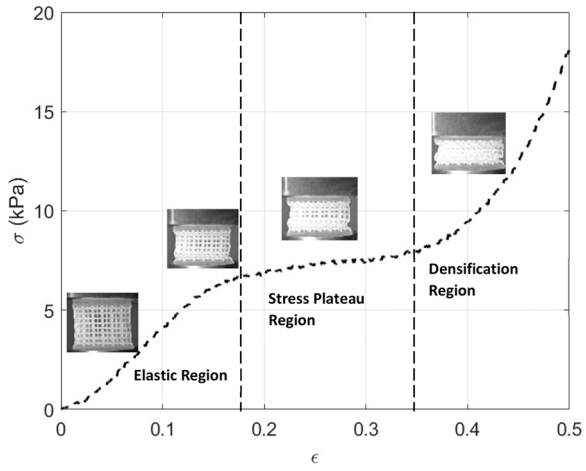

Fig. 4. Stress-strain curve of the sample structure under quasi-static compression. The curve exhibits 3 phases as noted.

specific parameters regarding properties of the structure can be obtained [23]. Given that the properties of most interest for this investigation are the elastic modulus, maximum yield stress and energy absorption capacity, it is the elastic and plateau phases which are the regions of significance. Therefore, these are also the regions where the effects of the modification of the internal design of the structure is most interesting.

2.2. Core modifications

In order to influence the behaviour of the structure in the early phases of its compression, different variations of column design in terms of density and shape are chosen to be implemented at the core of the structure. One of the expected effects of the core column is to provide additional resistance to compression and hence increase yield stress for the structure under short, weak impact scenarios while during stronger impact cases it will buckle and exhibit strain softening behaviour before continuing on to the plateau face in the similar manner as the core-less lattice.

2.2.1. Single cores

Two density variations of the core struts are considered, a solid column and a hollowed-out version of the same design (as shown in Fig. 5). The modification was implemented by removing four central unit cells from each layer of the base lattice (a column of $2 \times 2 \times 4$-unit cells) and replacing it with the column struts of the same dimensions in its top cross-sectional area and length. In order to further investigate the effects of the variation in the column strut itself, a two-level variant is also studied. Throughout the paper, the two shape variants of the core struts will be referred to as 'L1' and 'L2' as shown in Fig. 5.

2.2.2. Embedded cores

Further modifications are explored by considering an 'embedded' configuration, where 1-unit cell thick struts of the same design are placed at several parts of the re-entrant honeycomb core. Fig. 6 presents the isometric view of the single-core and the embedded-core modifications. Both hollow and filled versions as well as the L1 and L2 are considered for this configuration as well. Due to the thinner dimensions of the struts, the embedded configuration is expected to have less influence on the initial stiffness and the yield stress of the structure, however the collective behaviour of the struts could still provide added resistance to the lattice. Fig. 7 presents how each of the speciment types are classified with assigned code names with regards to the core type added and their arrangements within the lattice.

Table 2 lists the re-entrant honeycomb sandwich structure and all of its modifications investigated in this study. Percentage relative density are also presented, where the relative density is the mass-density of each of the lattice in proportion to the bulk density of the same material. The values for each specimen were calculated as the mean of 5 repeat measurements (of 5 separate samples) of the volume and mass, with the uncertainty obtained as the standard error of the mean. The filled core variations have higher relative density than their hollow counterparts as expected.

2.3. Fabrication of samples

Once the designs are finalised, the specimen are manufactured with a stereolithography 3D printing process using a Formlabs Form2 printer as outlined in Section 1. The STL files were uploaded onto the printer using Formlabs printing software Preform. The printer was set to closed mode to ensure optimal results are achieved using the vendor's resin. A Flexible 80 A cartridge was plugged into the printer and allowed to automatically fill a Form2 Resin Tank LT. Once the resin tank was full

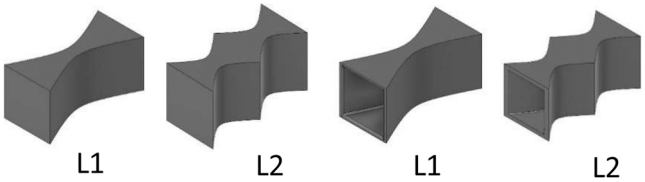

Fig. 5. The density and shape variant designs implemented to the modified re-entrant sandwich lattices.

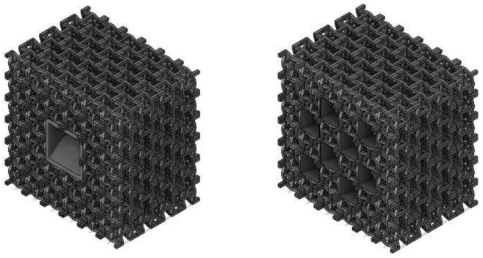

Fig. 6. Re-entrant core with the single core and embedded core of the hollow variant.

and the desired print temperature of 35 °C was achieved, the print was automatically started. The print settings are summarised in.
Table 3.

2.3.1. Flexible 80A resin

All of the test samples were printed in a urethane acrylate-based resin with brand name Flexible 80A, a proprietary product from Formlabs. According to the Flexible 80A safety data sheet provided by Formlabs, the resin composition is acrylate monomer(s) 75–95 w/w%, urethane dimethacrylate 3–6 w/w% and photo initiator(s) < 1.5 w/w%. This resin was chosen as it exhibited the most adequate balance between compressive flexibility and compatibility with the highly precise design in comparison to other candidates with similar soft, and flexible properties.

2.3.2. Fabrication process

One challenge of additively manufacturing the proposed designs was that the struts within the re-entrant honeycomb structure were substantially small in size and hence required additional consideration during the printing process, especially with the choice of a relatively soft resin material. Therefore, the fabrication process began with initial test printing to observe the suitability of the chosen resin with the desired design parameters in terms of precision as well as structural integrity. The prints were carried out with 0.1 mm layer thickness and the orientation of the designs on the build platform were adjusted to reduce any potential failures during the printing process due to the adhesion of the resin bath as it comes into constant contact.

The completed prints were then removed from the build platform with a metal spatula and any excess resin on the samples were rinsed using Formwash (Formlabs) isopropyl alcohol (IPA) bath for 10–12 min. Additional thorough washing with the IPA was often needed to remove the remanent resin from the small gaps in the unit cells. The samples were then placed in Formcure (Formlabs) UV post-curing chamber for 10 min at 60 °C to ensure the material reaches its optimal mechanical properties.

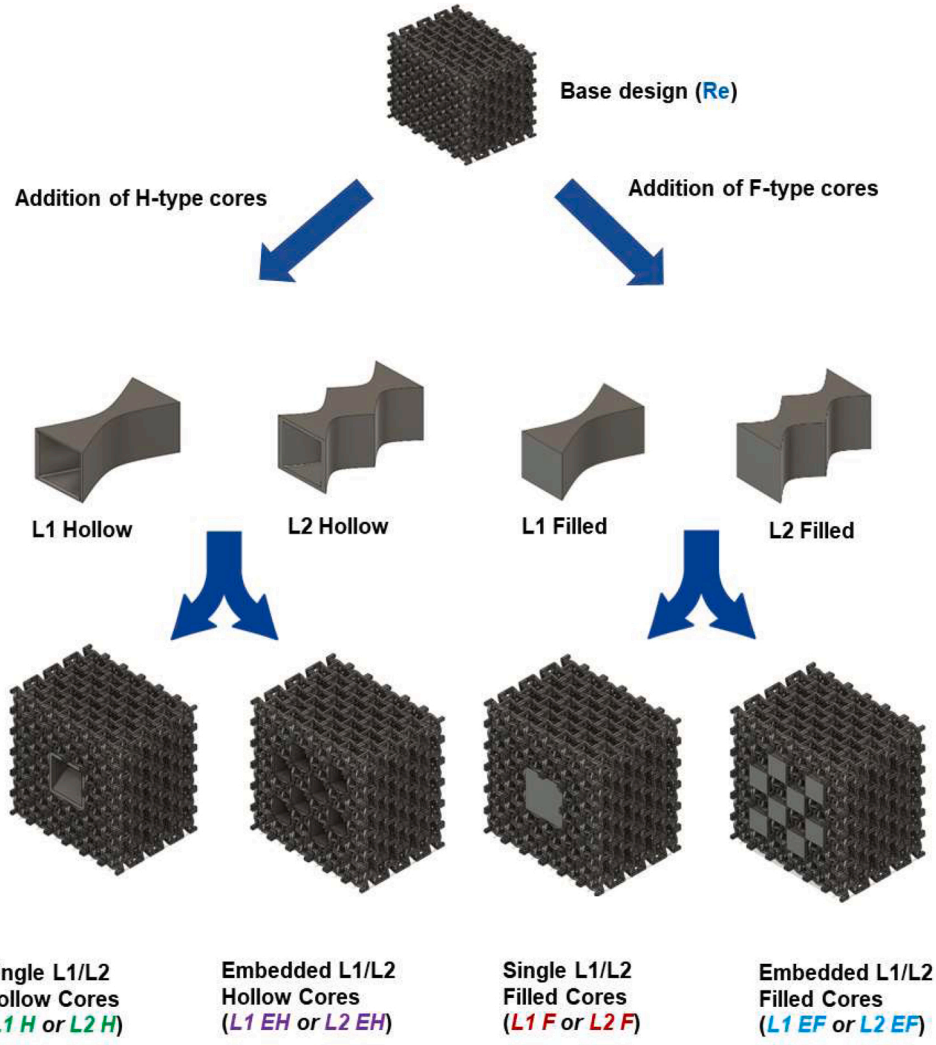

Fig. 7. Diagram outlining classification of each specimen with regards to the type of core added and the arrangements within the base lattice.

Table 2
Table of all variants of the re-entrant sandwich structures and their relative densities.

Specimen Type	Code Name	Relative Density (%)
Coreless Re-entrant	Re	26.50 ± 1.01
Hollow Single Core L1	L1H	29.09 ± 1.14
Filled Single Core L1	L1 F	32.72 ± 1.13
Hollow Embedded Core L1	L1 EH	30.33 ± 1.18
Filled Embedded Core L1	L1 EF	34.51 ± 1.16
Hollow Single Core L2	L2H	28.04 ± 2.03
Filled Single Core L2	L2 F	31.51 ± 4.19
Hollow Embedded Core L2	L2 EH	32.62 ± 1.99
Filled Embedded Core L2	L2 EF	35.35 ± 1.45

Table 3
Settings for the printing and post-curing processes.

Printer settings	
Laser type	Flexible 80A
Open/ closed mode	Closed
Layer height	100 μm
Bed temperature	35 °C
Wiper	Enabled
Auto-supports	Off
Post-cure settings	
Formwash	10–12 mins in IPA
Formcure	10 mins at 60 °C

2.3.3. Optimisation

During the printing and post-cure processes, some problems were observed. The samples that were printed separately were easily damaged while removed from the platform and rinsed within the bath. During the post-cure, deformation in the edges of the lattices were observed as the whole structure contracted in size.

In order to address these issues, the lattices were arranged in a strip, where four lattices were bound together between the long panels with thicker blocks on either end. The strip configuration was modelled in Fusion 360 (Autodesk) as shown in the left image of Fig. 8. Circular cut-outs were implemented to the strip panels for easier washing of the resin and separating the lattices at a later stage. The post-cured strips were then cut into separate samples.

The final dimensions of the printed samples were 18.3 ± 0.2 *mm* in thickness and 417.4 ± 8.8 mm^2 in area. The deviation in the values were due to minor loss of the features of the samples during the post-curing and cut-out processes.

2.4. Experimental methodology

To investigate the mechanical behaviour of the additively manufactured lattices under different compression conditions, two types of uniaxial compression apparatus were utilised, each appropriate for the required testing conditions and equipped with the relevant data acquisition diagnostics. For each experiment, the samples were loaded in the direction of top-panel to the bottom-panel of the sandwich structure, with displacement continuing up to densification of the structure. The analysis of internal structural damage and failure modes were carried out visually by post- processing sequences of images captured during each experiment.

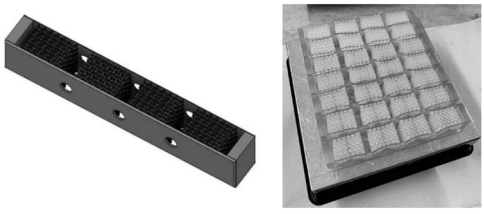

Fig. 8. The optimised strip configuration to minimise damage during additive manufacturing processes.

2.4.1. Low-rate system

A uniaxial Universal Testing Machine (UTM) was used for the quasi-static and intermediate compression tests, at strain rates in the range of 10^{-3}–1 s^{-1}. For this study, the specific apparatus was an *Instron 5982*, which comprises a stiff internal reaction frame and a crosshead that is electromechanically translated.

The *Instron 5982* (Fig. 9) incorporates a 100 kN capacity load cell fitted to the underside of the crosshead. The latter is electromechanically lowered onto the sample for compression and the position is continuously monitored. Both of the plates are stainless steel. The translation rate of the crosshead was set to be 5 mm/min for quasi-static and 1000 mm/min for intermediate rate in order to achieve the desired strain rate for the average sample thickness. The force history from the load cell and the displacement and time history from the motor encoder are recorded and displayed in real-time by the integrated computer system which controls the apparatus.

2.4.2. High-rate apparatus

For testing at 10^2 s^{-1} strain rates, a drop-weight impact test system was used. This type of apparatus is capable of much higher translation rates than the available UTM. The drop-weight system used in this study was an *Instron Dynatup 9250HV* (Fig. 10) with maximum impact velocity of 16 ms^{-1}. The highest velocity used in this study was 2 ms^{-1} and the drop-weight mass was 6.7 kg.

The *Instron Dynatup 9250HV* incorporates a load-cell in the drop-weight, positioned just above the impact face. This effectively monitors the force decelerating the part of the drop weight above it and with an appropriate correction indicates the force applied to a specimen being impacted. Furthermore, this record can be used calculate the deceleration, velocity, and displacement history. While this approach can usefully record force histories up to 220 kN in other applications, the force sensitivity required for this study (a force plateau of a few N) precludes it use. A force history more representative of that experienced by the specimen is best monitored as that passed through it, by a load cell placed beneath it. The relatively large displacements expected can be readily determined by analysis of high-speed imaging.

A bespoke load-cell was designed and manufactured for this study (Fig. 11). The solid cylindrical body was necked (reduced to 12 mm diameter) to reduce the cross-section area and aluminium-alloy (rather than steel) selected as a material in order to maximise strain and therefore the Wheatstone bridge output from strain-gauges. A Fylde H379TA dynamic bridge amplifier was used at an extreme gain of 10,000 to provide an estimated signal of 17 milli-volts/N. This was confirmed by calibration of the completed system (using the *Instron 5982*) to be 58.2 N/V. In order to protect the load cell from the much higher forces required to ultimately bring the drop-weight to rest, it was flanked by steel struts, each topped by 3 mm thick hardboard.

Each experiment was observed by a Vision Research Phantom V611 high-speed camera, running at its maximum full frame rate of 6200 fps. This was coupled to a high-rate data-acquisition device, NI USB-6361, which monitored the voltage signal from the Fylde H379TA. By this means, the load-cell signal was recorded with each frame of the video, thus providing precise synchronisation. A speckle pattern appropriate for digital image correlation (DIC) was applied to the visible perimeter of the impact head, allowing the displacement of the drop-weight to be tracked and used to calculate specimen strain. The high-speed image sequences were also useful in the qualitative assessment of specimen behaviour.

2.4.3. Data reduction

A MATLAB code was developed to automate the management and analysis of the acquired data from the experimental platforms. The analysis tool of the code calculated the parameters essential for material

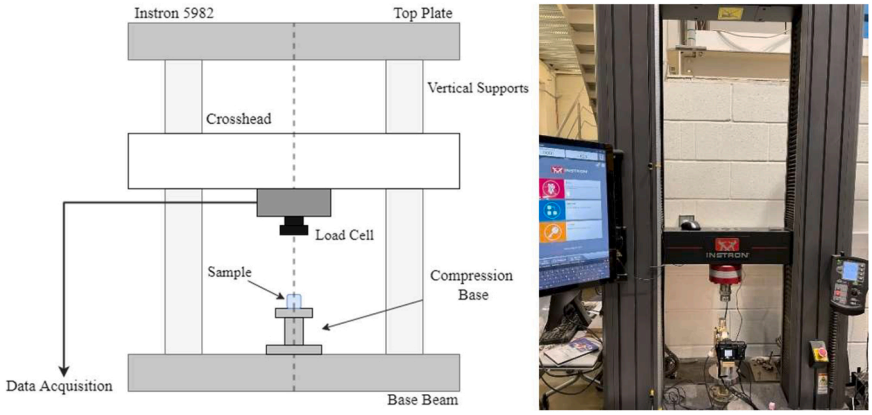

Fig. 9. Schematic of the Instron 5982 UTM and a photograph of the apparatus during testing.

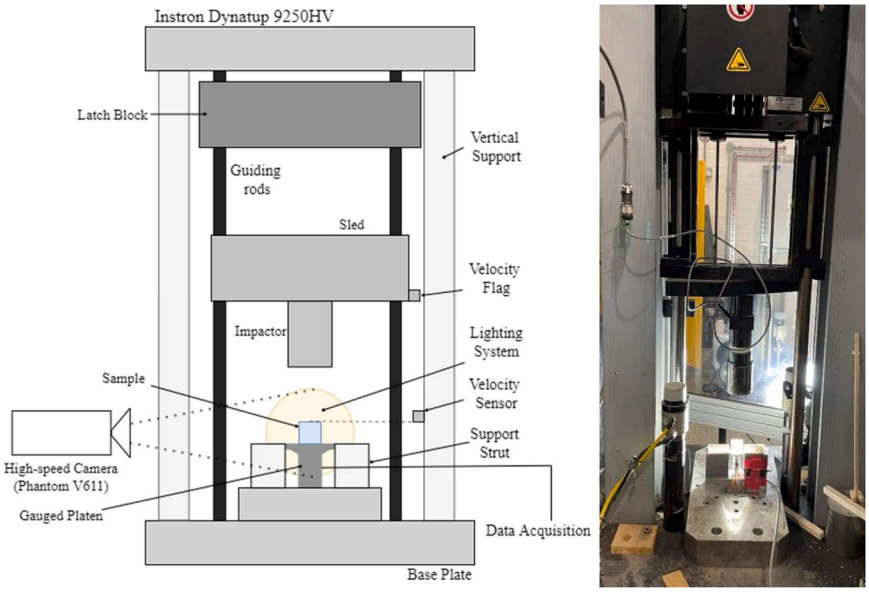

Fig. 10. Schematic of the Instron Dynatup 9250HV Drop-tower system and a photograph of the rear view of the apparatus with a sample in place ready for testing.

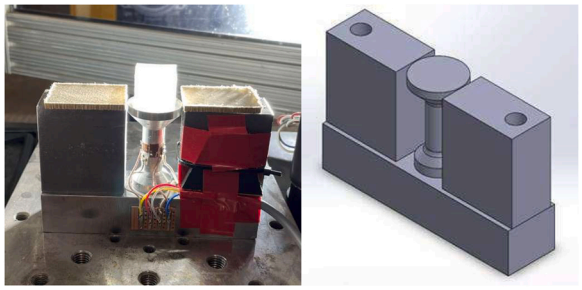

Fig. 11. Gauged platen configuration to provide a more sensitive force diagnostic. The steel struts either side protect the platen as the impactor is brought to rest.

characterisation such as stress, strain, and elastic modulus.

The main parameters of interest for this study are the engineering stress (σ) and engineering strain (ϵ), which are defined as:

$$\sigma = F/A \tag{1}$$

$$\varepsilon = \Delta L/L_0 \tag{2}$$

where F is the force applied to the sample, A is the sample cross-section, ΔL is the change in the sample length during compression, L_0 is the initial length of the sample before compression.

Elastic modulus can be obtained to characterise the material response in the early phase of the compression, given by:

$$E = \sigma/\varepsilon \tag{3}$$

in this case, the elastic modulus is computed graphically from the gradient of the stress-strain plot, such as shown in Fig. 4, produced by the analysis code.

Further parameters can be obtained, mainly the plateau stress and the energy absorption capacity calculated from the material response during stress plateau phase, which is a characteristic behaviour of cellular structures such as the lattices investigated in this study, as the unit cells begin to collapse. The parameters are defined as:

$$\sigma_p = \frac{\int_{\varepsilon_0}^{\varepsilon_D} \sigma(\varepsilon)d\varepsilon}{\varepsilon_D - \varepsilon_0} \tag{4}$$

$$W = \int_0^{\varepsilon_D} \sigma(\varepsilon)d\varepsilon \tag{5}$$

where σ_p is the plateau stress, ε_D and ε_0 are densification strain and the plateau strain respectively, and W is the energy absorption per unit volume up to densification of the structure. These parameters characterise the performance of the structure in protective and energy absorbing applications, and therefore the comparison of the values for each of the design modifications will be the main discussion of this study. One thing to note is that the plateau stress level is dependent on strain rate [11], and this would be another observation to be discussed between the three different rates of loading this study will investigate.

2.4.4. DIC analysis

The sequences of images recorded by the high-speed camera during the drop-weight tests were analysed to obtain displacement data, in order to calculate the strain history of the sample. The DIC analysis was carried out using Sandia National Laboratories DICe in 'tracking' mode [24]. A subset of the speckle pattern applied to the incoming edge of the impactor head was delimited as the Region of Interest (ROI) and tracked (Fig. 12). The ROI was selected such that it was at the same distance from the camera as the face of the specimen, thus minimising perspective error. It was not possible to track the surface of the specimen itself as this deformed substantially during compression and significantly changed in appearance.

3. Results and discussion

3.1. Stress-strain curves

Each of the samples listed in Table 2 are tested under three different strain rates of *0.005*, *1*, and *100* s^{-1} utilising the appropriate apparatus described in the previous section. For each strain rate, three repeat measurements of stress and strain (of three separate samples) were made per sample type. The representative stress and strain for each sample type were calculated as the mean of the three measurements as presented in Fig. 13, with the uncertainty obtained as the standard error of the mean. Fig. 13, presents the set of curves are divided in terms of *hollow* and *filled* variations for three different strain rates.

Firstly, it is observed that the 'core-less' reference lattice (Re) exhibit the three main deformation regions as mentioned 2.1.3 across the three compression rate regimes: 1) approximately linear elastic region up to around strain of 0.1; 2) followed by a plateau region of constant level of stress due to unit cell collapse up to around 0.4 deformation; 3) lastly, the densification phase characterised by sharp rise in the stress as most of the internal structures have collapsed [11,25,26].

The behaviour resembling that of bending-dominated deformation of cellular structures is as expected and the post-image analysis as shown in Fig. 14 further confirms this as the struts are observed to deform by elastic bending [10]. As the other test samples involve replacement of columns of unit cells within the Re structure with different core types, the general compressive behaviour of the different 'cored' structures is expected to be the combination of the response of the core and the Re structure. Therefore, any deviation from the Re curve can be viewed as due to the core columns.

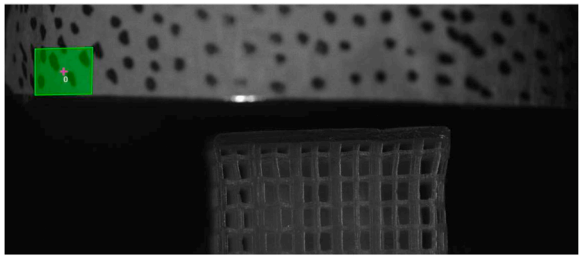

Fig. 12. First image of the recording of a drop-weight test. The speckle-pattern is visible on the impactor as it approaches the sample. The green box is the ROI which is tracked in the subsequent images.

3.1.1. Hollow core structures

The H-type samples of both single core and embedded core configurations show similar stages of deformation across all compression rates as reported in Fig. 13. The notable deviations from the Re curve are the plateau stress and strain, where the peak stress before the onset of cell collapse is mostly higher than that of Re.

While there are no well-defined trends between the proportional increase of plateau stress or the strain from that of the reference structure across the three strain-rates it is demonstrated that, in general, the inclusion of the hollow core struts increases the overall strength of the structures while maintaining the deformation mechanism. This may be pertained to the shape of the core structure with a different mode of deformation to the surrounding layers of re-entrant honeycomb unit cells. The image analysis of the test suggests this as the top and the bottom base section of the core folding axially as the neck bends (Fig. 15 (a)). This is unique to the single hollow core as the thinner embedded cores bend laterally as outlined in Fig. 15 (b).

Fig. 14 outlines the deformation of the Re, single core and embedded core structures. It is shown that while both Re and the single core maintain their lateral dimensions, the embedded core protrudes laterally due to the bending of the core struts, pushing out the surrounding layers (Fig. 15 (b)).

Although the observations do not highlight any significant differences between the single and the embedded configurations of the core struts, the results consistently indicates that the L2 variant reach higher peak stress than the L1 cores. This again may be attributed to the specific shape of the core as well as the volume of air within the L2 core.

3.1.2. Filled core structures

For the F-type samples, the similar responses are observed in terms the strain rate sensitivity and the L2 variants reaching higher stress levels than L1. However, the F-type samples present drastically modified behaviour from the base Re structure as well as notable differences between the single and the embedded cores. There are also variations across the different compression rates.

At 0.005 s^{-1} compression as shown in Fig. 13 (a), the single cores of both shape variants exhibit a response very similar to the 'stretch-dominated' architecture with relatively high moduli and yield stresses compared to their H-type counterparts before post-yielding softening response [10]. Instead of the plateau region, a basin region is characterised as the densification strain is reached. While a typical stretch-dominated behaviour is due to the fully triangulated unit cells in a structure [27], in the case of the single core F-type samples in this study the apparent high yield strength is due to the solid core strut within the structure and the post-yielding softening is due to the bending, or buckling at higher strain rates, of the core at the neck of the strut.

The difference in the deformation mode of the single hollow core and the filled core can be observed in the transverse strain of the structure during compression as shown in Fig. 16. As the hollow core bends axially ('folding'), the filled core bends laterally, causing the transverse dimension of the lattice to 'bulge out' near the densification. In the case for the embedded cores, the effects of the solid struts are less evident due to the smaller size, and they are observed to bend in the same manner as their hollow counterparts, however they reach the densification phase earlier (Fig. 13 (c)) as the thickness of each filled struts constrain further compression of the structure.

At higher compression rates, the responses of the single cored samples are dominated by the core struts and the behaviour seems to progress from the initial elastic phase to the densification, bypassing any post-yield softening phases (Fig. 13(b) and (c)). This observation could be due to the duration of the loading was too short for the structure to fully respond. However, this also indicates that these design iterations are not suitable in scenarios with these types of loading. In the case of

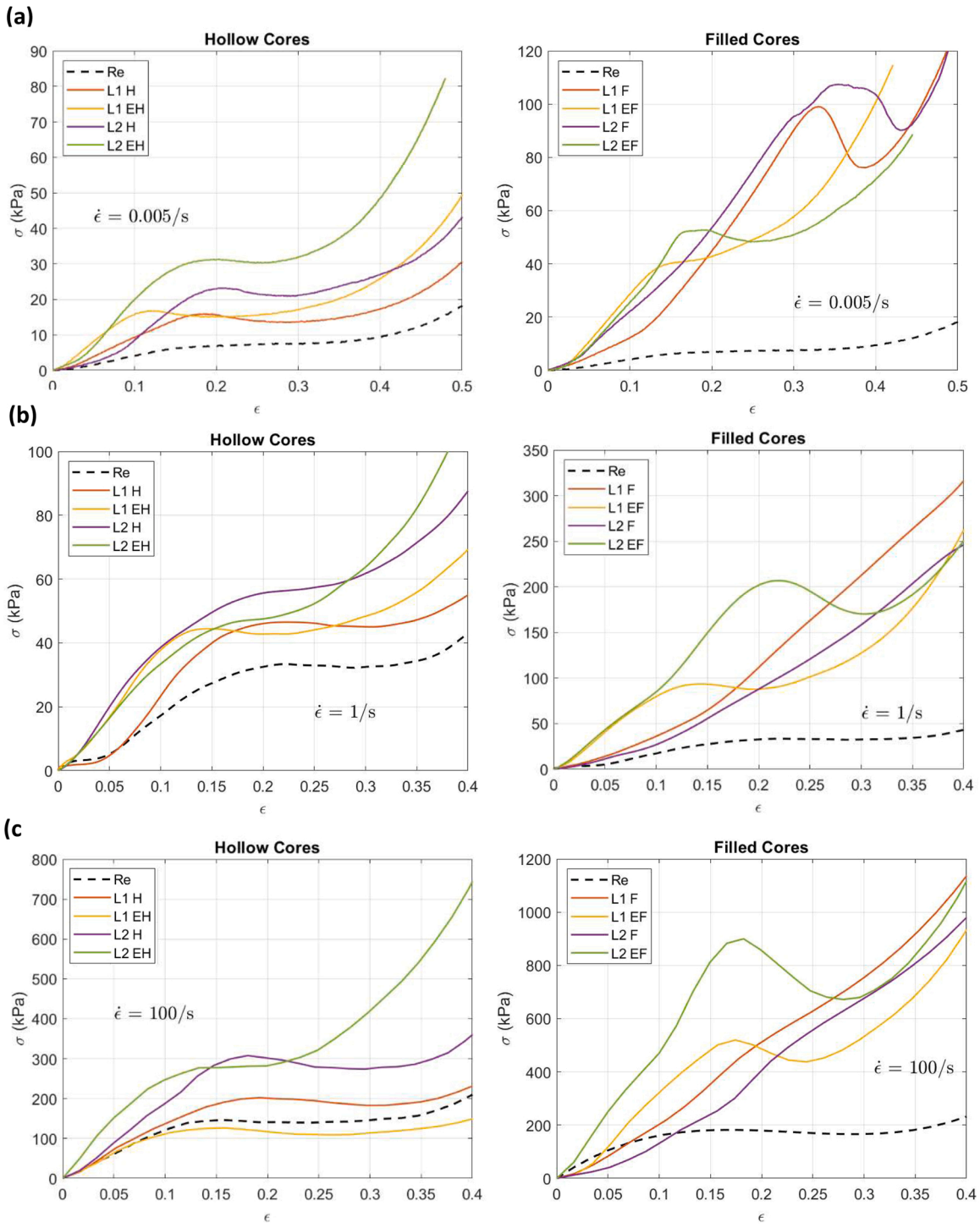

Fig. 13. Stress-strain curve comparison of the hollow and filled cores across three different strain rate compressions.

the embedded versions, the shapes of the curves are maintained with the peak stress increasing with the compression rates.

3.2. Parameters of interest

The key parameters of interest in this study were calculated following the equations outlined in Section 3.3.1. The parameters were calculated as the mean value from the stress-strain curves of 3 repeated experiments, with the uncertainty represented as the standard error of the mean. Table 4 summarises the calculated values and the associated uncertainties for each of the sample types. The values for plateau stress and energy absorption capacity are not included for sample types L1 F and L2 F as they did not exhibit the characteristic deformation for cellular structures as shown in Fig. 13(b) and (c).

The strain sensitivity of the three parameters is presented as semi-log plots in Fig. 17. For each of the parameters the samples are divided into the two shape variants (L1 and L2), with the linear interpolation line through the data points for the reference structure, Re, as the reference line. The plots in Fig. 17, represents a viscoelastic behaviour where the structures exhibit strain hardening. Furthermore, in general, the core implemented samples show increased elastic moduli compared to the coreless structure Re. This result indicates that the core struts provide

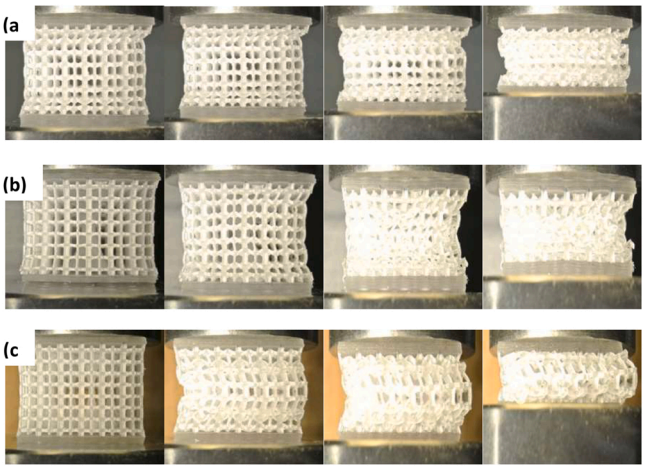

Fig. 14. The stages of compressive deformation of H-type (hollow core) samples: (a) Core-less reference; (b) Single core; (c) Embedded core.

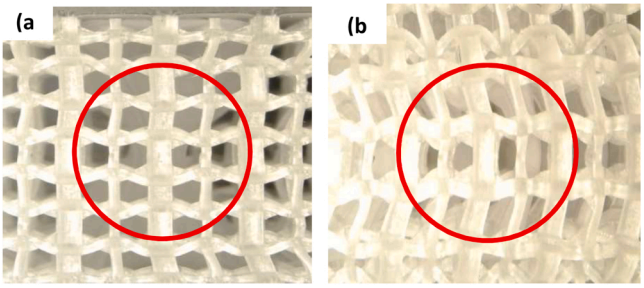

Fig. 15. Deformation modes of the core struts: a) Single hollow core; b) Embedded core. The single hollow core deforms by 'folding' axially while the embedded struts bend laterally.

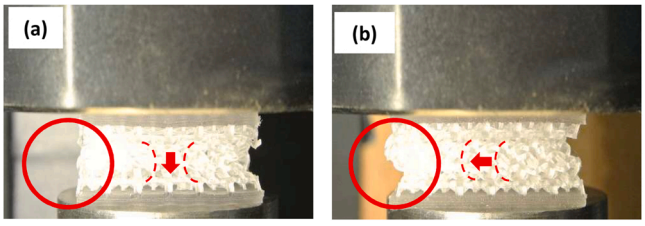

Fig. 16. Comparison of the single H core vs F core: (a) Hollow core shows negligible transverse strain as the core bends axially; (b) Filled core exhibits a 'bulge' due to the core bending laterally.

the structures with 'additional stiffness'.

At lowest, quasi-static, rate all of the samples exhibit similar behaviour with the F type samples indicating highest strength. At 1 s^{-1}, despite the spread in the elastic moduli, most of the sample types exhibit near quasi-static response in terms of the plateau stress and the energy capacity, with small deviation from the values at 0.005 s^{-1}. At the 100 s^{-1}, the values spread out more significantly, with the EF, embedded-filled core, observed to have a drastic increase in all parameters.

With regards to the differences between the L1 and L2 variants, the behaviour in the lower strain rates is very similar for both variants, and the closeness of the values are reported for both. For L2, the F type samples exhibit more noticeably higher values across all strain rates, and the spread in the values between the sample types are more evident at the highest strain rate.

Table 4
Summary of calculated parameters for each specimen types under uniaxial compression.

Specimen	$\dot{\epsilon}(s^{-1})$	E (kPa)	σ_p(kPa)	W (kJm^{-3})
Re	0.005	55 ± 9.7	10 ± 3.1	1.943 ± 0.3
	1	217 ± 78.6	43 ± 10.7	8 ± 1.4
	100	1546 ± 18.9	204 ± 31.9	48 ± 4.5
L1H	0.005	133 ± 22.8	19 ± 4.5	4 ± 0.7
	1	467 ± 165	70 ± 24.7	13 ± 4.3
	100	1677 ± 108	266 ± 26.5	59 ± 9.7
L1 F	0.005	477 ± 74.7	125 ± 18.4	19 ± 3.8
	1	671 ± 89.1	-	-
	100	2651 ± 142	-	-
L1 EH	0.005	204 ± 22.9	22 ± 3.5	5 ± 0.6
	1	468 ± 86.1	56 ± 17.9	9 ± 1.3
	100	2967 ± 49.3	368 ± 34.5	67 ± 4.7
L1 EF	0.005	421 ± 39.1	59 ± 11.9	9 ± 1.2
	1	889 ± 208	185 ± 11.1	28 ± 16.9
	100	4988 ± 114	617 ± 20.1	93 ± 2.4
L2H	0.005	262 ± 109	33 ± 12.4	6 ± 2.1
	1	501 ± 60.1	86 ± 53.9	15 ± 7.1
	100	2438 ± 57.6	391 ± 80.2	79 ± 5.8
L2 F	0.005	580 ± 193	166 ± 120	28 ± 11.7
	1	324 ± 22.3	-	-
	100	2207 ± 276	-	-
L2 EH	0.005	318 ± 40	40 ± 2.8	7 ± 1.08
	1	413 ± 80.4	68 ± 3.37	11 ± 0.81
	100	3381 ± 99.4	356 ± 76.3	52 ± 7.84
L2 EF	0.005	429 ± 27.7	65 ± 9.91	10 ± 1.98
	1	1021 ± 88.8	243 ± 40.1	43 ± 13.1
	100	5836 ± 166	1005 ± 40.7	173 ± 27.9

3.3. Applications and functionality

While the key aim of this study is to investigate the variations in the responses of the structures as one specific component of the architecture are modified, it is also of interest to compare the characteristics of each sample variants and discuss the viability and the capabilities of each in the applications of the scenarios similar to the conditions produced in the experimentation.

The H type designs can be used as direct enhancement of the core-less Re structure, as they maintain the shape of the response curve with increased yield stress and energy absorption capacity. These types of structures may be deployed in areas where high energy absorption with structure deformation is needed at relatively low stress levels. Such applications would include protection of soft or fragile subjects from vibrations and loading such as in automotive and aerospace. The characteristics of the structures being small and light-weight are also main design objectives in these fields [27]. While the single core F types are not suitable candidates for effective energy absorbing structures at high-rate compressions, the embedded configurations exhibit responses that have potential viability in situations where light-weight structures with high stiffness and strengths are required. One possible proposed arrangement could be a combination of the H types and the EF designs layered axially. Such arrangement can provide functional flexibility, where it can perform adequately under a range of loading types. At low stress levels, the H-layers will deform and provide sufficient protection while still maintaining the general structure of the arrangement due to the strength provided by the EF-layer. Under stronger impacts, after the initial deformation of the H-layer, the EF-layer will provide with additional mitigation due to the higher yield stress and the post-yield softening.

4. Conclusions

This study has successfully presented the development process of lightweight lattice structures using the vat photopolymerisation with a soft, flexible material. Structures that are small yet have highly precise design features were manufactured and various core design iterations

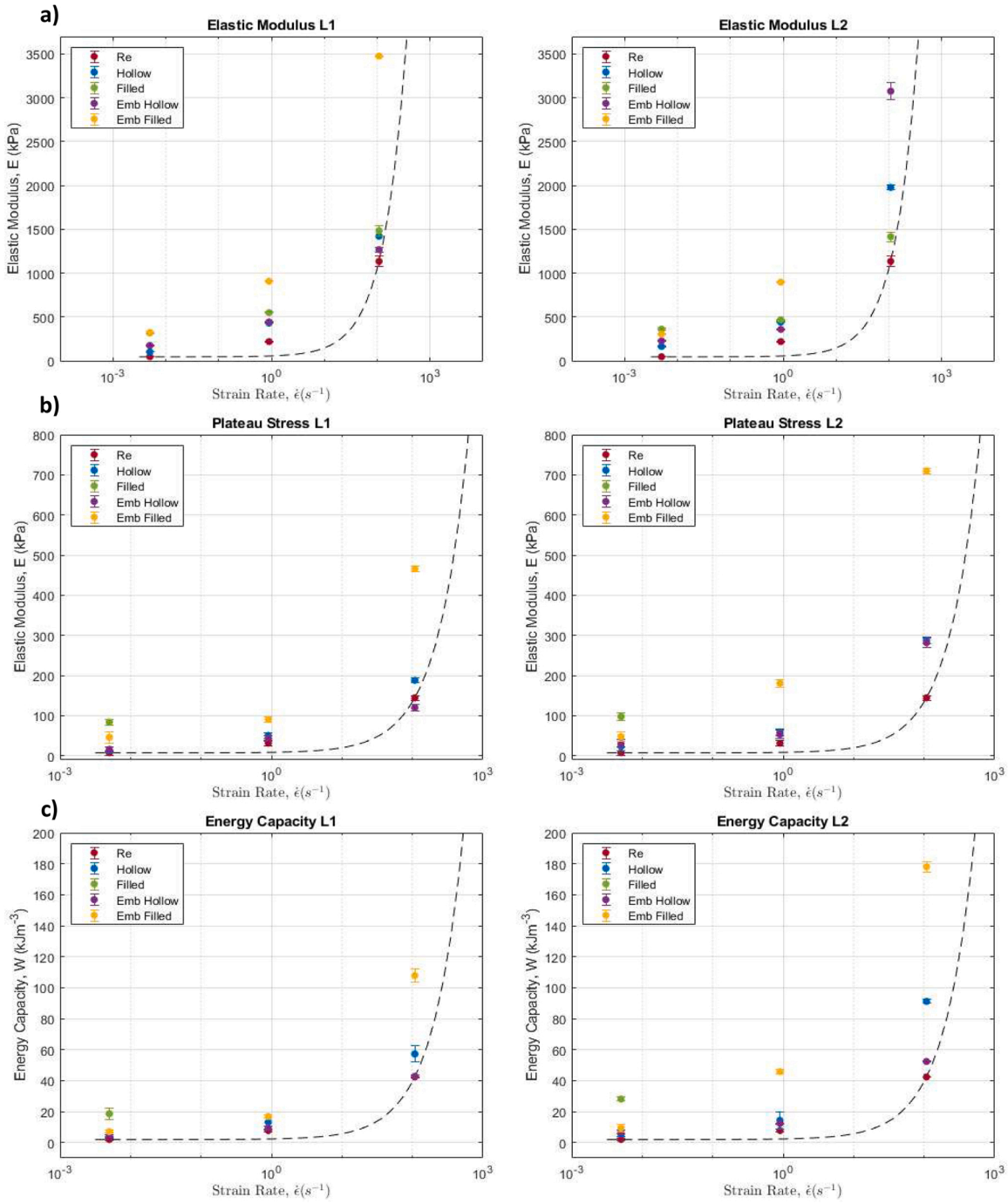

Fig. 17. Semi-log plots of a) Young modulus; b) plateau stress; c) energy absorption capacity strain rate sensitivity.

were implemented, demonstrating the flexibility and accessibility of the additive manufacturing process.

Compression tests across three strain rates on the printed samples have yielded distinct responses, suggesting that the implementation of the cores result in higher strength and energy absorption per unit volume in comparison to the reference structure. Based on the response curves and the calculated parameters, the H type designs are viable as enhanced versions of the core-less re-entrant honeycomb sandwich structure. At high strain rates, the single F type cores are not viable due to the lack of post-yield reduction in stress level, but the embedded configurations can be used for high stiffness, short duration loading situations. Alternatively, a combination of H types and EF type, either layered on top of each other or included within the same construct could be considered. Based on the results, the combined structure would be able to address situations where the incoming loads can vary in terms of duration and magnitude within a single application. Suitable example of this would be, as previously mentioned, in driver seats of racing cars and various aerospace scenarios.

The findings have revealed that the properties of the core struts have significant effect on the overall behaviour and the properties of the structure. While only two parameters, density, and shape, of the core are considered in this study, it offers a possibility of vast design modifications that may be considered in future studies.

CRediT authorship contribution statement

James Lee: Conceptualization, Methodology, Investigation, Analysis, Writing – review & editing. **Ali Mohammed:** 3D printing and assistance in sample preparation, Writing – review & editing. **Andy Pullen:** Experimental design and Supervision, Assistance in data acquisition and analysis, Writing – review & editing. **Connor Myant:** Conceptualisation, Writing – review & editing, Supervision. **William Proud:** Conceptualisation, Writing – review & editing, Supervision.

Declaration of Competing Interest

The authors declare that they have no known competing financial interests or personal relationships that could have appeared to influence the work reported in this paper.

Data Availability

Data will be made available on request.

Acknowledgements

This work is supported by the EPSRC DTP Grant, UK and Imperial College London, UK. Authors would like to acknowledge Prof. Mansoor A. Khan for advice on epidemiology of spinal injuries in elite motor sports and Mr Pablo Durán Millán for assisting during 3D printing and schematic design.

References

[1] B.K. Nagesha, V. Dhinakaran, M. Varsha Shree, K.P. Manoj Kumar, D. Chalawadi, T. Sathish, Review on characterization and impacts of the lattice structure in additive manufacturing, Mater. Today: Proc. 21 (2020) 916–919.
[2] W. Tao, M.C. Leu, Design of lattice structure for additive manufacturing, 2016, Int. Symp. . Flex. Autom. (ISFA) (2016) 325–332.
[3] K. Ahmed, A.Q. Malik, Experimental investigations of the response of a portable container to blast, fragmentation, and thermal effects of energetic materials detonation, Int. J. Prot. Struct. 13 (1) (2021) 45–64.
[4] R.R. Boyer, J.D. Cotton, M. Mohaghegh, R.E. Schafrik, Materials considerations for aerospace applications, MRS Bull. 40 (12) (2015) 1055–1066.
[5] A.I. Taub, A.A. Luo, Advanced lightweight materials and manufacturing processes for automotive applications, MRS Bull. 40 (12) (2015) 1045–1054.
[6] F.P.W. Melchels, J. Feijen, D.W. Grijpma, A review on stereolithography and its applications in biomedical engineering, Biomaterials 31 (24) (2010) 6121–6130.
[7] J.S. Mohammed, Applications of 3D printing technologies in oceanography, Methods Oceanogr. 17 (2016) 97–117.
[8] R.J. Mondschein, A. Kanitkar, C.B. Williams, S.S. Verbridge, T.E. Long, Polymer structure-property requirements for stereolithographic 3D printing of soft tissue engineering scaffolds, Biomaterials 140 (2017) 170–188.
[9] B.T. Phillips, J. Allder, G. Bolan, R.S. Nagle, A. Redington, T. Hellebrekers, J. Borden, N. Pawlenko, S. Licht, Additive manufacturing aboard a moving vessel at sea using passively stabilized stereolithography (SLA) 3D printing, Addit. Manuf. 31 (2020), 100969.
[10] M. Ashby, The properties of foams and lattices, philosophical transactions, Philos. Trans. Ser. A Math. Phys. Eng. Sci. 364 (2006) 15–30.
[11] L.J. Gibson, Cellular solids, MRS Bull. 28 (4) (2003) 270–274.
[12] R. Gümrük, R.A.W. Mines, S. Karadeniz, Static mechanical behaviours of stainless steel micro-lattice structures under different loading conditions, Mater. Sci. Eng.: A 586 (2013) 392–406.
[13] C. Yan, L. Hao, A. Hussein, S.L. Bubb, P. Young, D. Raymont, Evaluation of light-weight AlSi10Mg periodic cellular lattice structures fabricated via direct metal laser sintering, J. Mater. Process. Technol. 214 (4) (2014) 856–864.
[14] C. Yan, L. Hao, A. Hussein, P. Young, D. Raymont, Advanced lightweight 316L stainless steel cellular lattice structures fabricated via selective laser melting, Mater. Des. 55 (2014) 533–541.
[15] B. Gorny, T. Niendorf, J. Lackmann, M. Thoene, T. Troester, H.J. Maier, In situ characterization of the deformation and failure behavior of non-stochastic porous structures processed by selective laser melting, Mater. Sci. Eng.: A 528 (27) (2011) 7962–7967.
[16] R. Gümrük, R.A.W. Mines, Compressive behaviour of stainless steel micro-lattice structures, Int. J. Mech. Sci. 68 (2013) 125–139.
[17] S. Merkt, C. Hinke, J. Bültmann, M. Brandt, Y. Xie, Mechanical response of TiAl6V4 lattice structures manufactured by selective laser melting in quasistatic and dynamic compression tests, J. Laser Appl. 27 (S1) (2015) S17006.
[18] R. Lakes, Foam structures with a negative Poisson's Ratio, Science 235 (4792) (1987) 1038–1040.
[19] Y. Prawoto, Seeing auxetic materials from the mechanics point of view: a structural review on the negative Poisson's ratio, Comput. Mater. Sci. 58 (2012) 140–153.
[20] V. Salit, T. Weller, On the feasibility of introducing auxetic behavior into thin-walled structures, Acta Mater. 57 (1) (2009) 125–135.
[21] R. Almgren, An isotropic three-dimensional structure with Poisson's ratio _ 1, J. Elast. 15 (1985) 427–430.
[22] J.V. Mane, S. Chandra, S. Sharma, H. Ali, V.M. Chavan, B.S. Manjunath, R.J. Patel, Mechanical property evaluation of polyurethane foam under quasi-static and dynamic strain rates- an experimental study, Procedia Eng. 173 (2017) 726–731.
[23] Z. Lanzhu, R. Dupuis, Measurement and identification of dynamic properties of flexible polyurethane foam, J. Vib. Control 17 (4) (2010) 517–526.
[24] S.N. Laboratories, Digital Image Correlation Engine (DICe), 2022. ⟨https://www.sandia.gov/ccr/software/digital-image-correlation-engine-dice/⟩ (Accessed August 2022 2022).
[25] S.Y. Choy, C.-N. Sun, K.F. Leong, J. Wei, Compressive properties of functionally graded lattice structures manufactured by selective laser melting, Mater. Des. 131 (2017) 112–120.
[26] T. Maconachie, M. Leary, B. Lozanovski, X. Zhang, M. Qian, O. Faruque, M. Brandt, SLM lattice structures: properties, performance, applications and challenges, Mater. Des. 183 (2019), 108137.
[27] M. Duan, C.E. Okwudire, Modeling and observer-based compensation of slip in a friction drive for servo positioning, in: Proceedings of the 2016 International Symposium on Flexible Automation (ISFA), 2016, pp. 45–52.